Preprint Cambridge Centre for Computational Chemical Engineering ISSN 1473 – 4273

Predicting power conversion efficiency of organic photovoltaics: models and data analysis

Andreas Eibeck[4], Daniel Nurkowski[1], Angiras Menon[2], Jiaru Bai[2], Jinkui Wu[3], Li Zhou[3], Sebastian Mosbach[1,2], Jethro Akroyd[1,2], Markus Kraft[2,4,5]

released: February 23, 2021

[1] CMCL Innovations
Sheraton House
Castle Park
Cambridge CB30AX
UK

[2] Department of Chemical Engineering
and Biotechnology
University of Cambridge
Philippa Fawcett Drive
Cambridge, CB3 0AS
United Kingdom

[3] School of Chemical Engineering
Sichuan University
Sichuan
China

[4] CARES
Cambridge Centre for Advanced
Research and Education in Singapore
1 Create Way
CREATE Tower, #05-05
Singapore, 138602

[5] School of Chemical
and Biomedical Engineering
Nanyang Technological University
62 Nanyang Drive
Singapore, 637459

Preprint No. 268

UNIVERSITY OF CAMBRIDGE

Keywords: organic photovoltaics, PCE, machine learning, neural networks, baseline models

Edited by
Computational Modelling Group
Department of Chemical Engineering and Biotechnology
University of Cambridge
Philippa Fawcett Drive
Cambridge, CB3 0AS
United Kingdom

E-Mail: mk306@cam.ac.uk
World Wide Web: https://como.ceb.cam.ac.uk/

Abstract

In this paper, the ability of three selected machine learning neural and baseline models in predicting the power conversion efficiency (PCE) of organic photovoltaics (OPVs) using molecular structure information as an input is assessed. The bi-directional long short-term memory (gFSI/BiLSTM), attentive fingerprints (Attentive FP), and simple graph (Simple GNN) neural networks as well as baseline support vector regression (SVR), random forests (RF), and high dimensional model representation (HDMR) methods are trained to both the large and computational Harvard clean energy project database (CEPDB) and the much smaller experimental Harvard organic photovoltaic 15 dataset (HOPV15). It was found that the neural-based models generally performed better on the computational dataset with the Attentive FP model reaching a state of the art performance with the test set mean squared error of 0.071. The experimental dataset proved much harder to fit, with all the models exhibiting a rather poor performance. Contrary to the computational dataset, the baseline models were found to perform better than the neural models. To improve the ability of machine learning models to predict PCEs for OPVs, either better computational results that correlate well with experiments or more experimental data at well-controlled conditions are likely required.

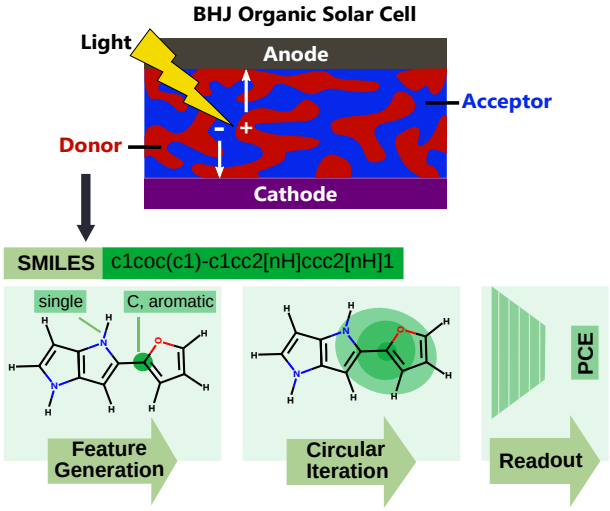

Highlights

- Neural and baseline models assessed for predicting PCE of organic photovoltaics.
- Computational (CEPDB) and experimental (HOPV15) literature datasets considered.
- The CEPDB fitted well by all models, but predicted PCEs disagree with experiments.
- The HOPV15 fitted poorly, with the baseline models being better than the neural models.

Contents

1 Introduction

With a strong global push towards clean energy generation, more resources are being invested in researching and developing photovoltaic devices. Whilst silicon-based solar cells remain the most prominent in the solar cell market, other materials have also been rapidly gaining interest, such as perovskite-based solar cells [11, 40] that have been seen to achieve promising power conversion efficiencies (PCEs)[15]. However, perovskite based cells are known to have environmental stability and processing issues [43]. As a consequence, organic solar cells (OSCs) have been gaining interest, due to their low weight, flexibility, environment stabilities, and ease of manufacture [3, 38, 48]. Although OSCs often have substantially lower PCEs [13, 38], recent synthesis efforts and theoretical predictions have suggested that OSCs could achieve conversion efficiencies that make them competitive with silicon and perovskite-based materials [33, 37, 51] with potential PCEs reaching as high as 20% [37], or even 30% [51] in some cases.

As conducting experiments can prove to be challenging both time and resource-wise, computational methods are often employed to enable rapid screening of candidate materials for organic solar cells based on PCE. Frequently, computational estimates of the PCE employ the widely used Scharber equation [38], which predicts the PCE of a given organic solar cell architecture from only a few key parameters, all of which can be determined by application of quantum chemical methods such as density functional theory (DFT). However, DFT calculations require substantial computational time that is not conducive to fast screening. Therefore, machine learning (ML) methods are often used to derive quantitative structure property relationships (QSPR) between the performance of the organic photovoltaic and the underlying properties of the materials, as they can make use of existing computational and experimental data and make predictions at a fraction of the cost.

A wide variety of machine learning algorithms have been applied to predict the performance of organic photovoltaics by using different target data sets. The Harvard Clean Energy Project Database (CEPDB) [13], is one such target data set for ML models that contains computationally determined PCE values for 2.3 million organic photovoltaic candidates. An example of ML methods being applied to the CEPDB is the artificial neural network (ANN) trained by Pyzer-Knapp et al. [29], who achieved good prediction accuracy for PCE and other molecular properties. Various deep learning models have also been applied, including the convolutional neural network of Sun et al. [41], who classified organic photovoltaic candidates into low performance (<5% PCE) and high performance (5-10%PCE) materials, as well as various graph neural network (GNN) approaches that directly predict PCE [9], [52], [34]. Recent approaches have integrated the attention mechanism, originally introduced for recurrent neural networks for machine translation [5], in order to improve performance by focusing on local substructures that are relevant for the prediction task. For example, Wu et al. [49] used attention to couple a Bi-Directional Long Short-Term Memory (LSTM, [14]) and multilayer perceptron (MLP) to predict PCE based on sequentialized molecular structure and fragment types. The authors achieved a very high degree of prediction accuracy on the CEPDB and identified functional groups that contribute towards a molecule having higher PCE.

However, it has been noted that computational predictions of PCE of OSCs often do not

agree well with experimental measurements, and that machine learning approaches like Gaussian process regression are necessary to improve agreement [13, 23, 30]. As a consequence, experimental OPV datasets, such as the Harvard Organic PhotoVoltaic dataset (HOPV15) [22], are often used to train ML methods instead. Examples include the k-Nearest Neighbours (k-NN) and Kernel Ridge Regression (KRR) models used for direct PCE prediction by Padula et al. [27], the ANN and RF methods used for classification by Nagasawa et al. [26], and the five ML models (MLP, Deep Neural network (DNN), Convolutional Neural Network, RF, and Support Vector Machine (SVM)) trained by Sun et al. [42]. In general, ML models perform worse on experimental data than the CEPDB, with better performing models reaching Pearson correlation coefficients r of 0.7. Given this, studies have also tried to include additional DFT-computed molecular descriptors in the ML models to improve performance on experimental datasets. This includes the training of RF, ANN, and gradient boosting regression trees by Sahu and Ma [35], Sahu et al. [36] in conjunction with 13 DFT derived molecular descriptors and 300 experimental PCEs, as well as the work by Zhao et al. [54], who trained SVM, k-NN, and KRR models with a variety of different DFT derived descriptors and 566 experimental PCEs. The performance of these ML models was similar, achieving correlations of $r = 0.7 - 0.8$, and suggests that including DFT descriptors achieves only a modest improvement, possibly due to many descriptors being implicitly linked to structure.

Ultimately, the goals of these works is to train an ML model that can accurately and quickly screen candidate OPV materials to identify potential high performance candidates for further characterization. Whilst it appears that several different ML approaches can achieve similar levels of performance, a crucial aspect is the choice of training data. Training to computationally determined PCEs has the advantage of large and standardized datasets with controllable and known degrees of freedom [24], but these PCEs correlate poorly to experimental measurements which can undermine their utility. However, training to experimentally characterized PCEs is harder due to the wide variety of experimental conditions, expected experimental errors, larger number of degrees of freedom and usually smaller amount of available data.

In light of these considerations, **the aim of this paper is** to critically test the ability of machine learning models to predict the PCE of organic photovoltaics based on the SMILES-derived molecular structure information, as well as assess the impact and implications of the choice of training data. To do this, three neural machine learning models are trained: the BiLSTM model used by Wu et al. [49], the Attentive Fingerprints (FP) used by Xiong et al. [52] and a simple Graph Neural Network (Simple GNN) that serves as an intermediate between these two models in terms of featurization included. Three baseline models: Random Forests (RF), Support Vector Regression (SVR), and High Dimensional Model Representation (HDMR) are also trained for comparative purposes. These six models are trained to predict PCE based on descriptions of molecular structure generated from SMILES strings and finger print analysis. In order to test the impact of training data, the six models are trained to both the large, entirely computational CEPDB, and the small, experimental HOPV15 dataset. Finally, the impact of the training data and choice of ML model on predicting PCEs that are ultimately useful for guiding organic photovoltaic design is critically assessed based on the training results.

2 Data

2.1 Harvard clean energy project dataset

The first major dataset used in this work is the Harvard CEPDB, developed originally by Hachmann et al. [13]. As mentioned previously, the CEPDB only contains computational results for approximately 2.3 million organic solar cell acceptor candidate materials. Whilst the original servers and websites for the CEPDB are no longer in use, the data can be accessed from the following website: https://www.matter.toronto.edu/basic-content-page/data-download. The CEPDB provides substantial data for training machine learning algorithms. The molecular structures in the CEPDB are generated from 26 different building blocks, as detailed in Hachmann et al. [13]. Each species in the CEPDB is assigned an ID, with the stoichiometry and SMILES string also provided to give the basic molecular structural information for the organic solar cell acceptor species. For each species, the PCE, the short circuit current density J_{sc}, the open circuit voltage V_{oc}, the HOMO energy, the LUMO energy, and the HOMO-LUMO gap are reported as computed by the DFT methods described by Hachmann et al. [13]. The PCE values reported in the CEPDB are computed using the Scharber equation:

$$\text{PCE} = \frac{FF\, V_{\text{oc}}\, J_{\text{sc}}}{P_{\text{in}}}, \tag{1}$$

where FF is the fill factor and P_{in} is the input power. Scharber et al. [38] also developed models for the various parameters in the Scharber equation, which are used to derive the CEPDB data. The fill factor, FF is assumed to be 0.65, and the open circuit voltage given by the following expression, derived by Scharber et al. [38]

$$V_{\text{oc}} = \frac{1}{e}\left(|E^{\text{Donor}}\text{HOMO}| - |E^{\text{Acceptor}}\text{LUMO}|\right) - 0.3, \tag{2}$$

with e as the electron charge, E^{Donor}HOMO being the energy of the highest occupied molecular orbital (HOMO) of the donor material in the cell, E^{Acceptor}LUMO similarly being the energy of the lowest unoccupied molecular orbital (LUMO) of the acceptor material in the cell, and 0.3 being an empirical correction. In the CEPDB, the acceptor is assumed to be PCBM, a class of fullerenic derivatives commonly used as electron acceptors in both hybrid perovskite and organic photovoltaic materials. The magnitude of E^{Acceptor}LUMO is assumed to be 4.3 eV, in accordance with experimental measurements [53].

The two remaining parameters in the Scharber equation, J_{sc}, and P_{in}, are both derived from the incident solar photon flux density, which essentially amounts to integrating the Air Mass 1.5 (AM1.5) spectra [12]. For this spectra, integrating the spectra across the wavelength gives a P_{in} of approximately 1000 W/m^2. The short circuit current density is given by:

$$J_{\text{sc}} = \text{EQE} \times e \int_{E_g}^{\infty} \phi_{\text{ph}}(E)\mathrm{d}E, \tag{3}$$

with the external quantum efficiency EQE set to 0.65 in the Scharber model, E_g as the band gap of the donor material, and ϕ_{ph} being the incident solar photo flux density as a function of the energy E.

The Scharber Model shows that computing PCE, V_{oc}, and J_{sc} only requires determining the HOMO and LUMO levels of the donor material in the OSC, which is readily derived from the quantum chemical calculations performed by Hachmann et al. [13].

Before implementing and training the various machine learning algorithms to the data in the CEPDB, the data is first pre-processed to understand the characteristics of the species in the CEPDB. First, all of the provided SMILES strings are checked to see if they are valid, in that they successfully encode a sensible molecular structure that can be identified by RDKit. In total 9821 invalid SMILES were identified and thus these species were removed from consideration for training purposes. Next, the maximum length of the valid SMILES, the maximum number of atoms in a single molecule in the data set, and the different atom types are identified, as these define the bounds of the structures that the machine learning methods will need to model. For the CEPDB, the maximum length of SMILES and maximum number of atoms in a single molecule are 83 and 53 respectively. There are seven different atoms in the CEPDB, namely C, H, O, N, Si, and Se. However, several atoms can be either aromatic or non-aromatic. This can significantly impact the underlying chemistry and molecular behaviour, which is another factor to be taken into account. A final layer of pre-processing is related to the reported PCE values, in which molecules with a PCE value smaller than the defined threshold value of 0.0001 are also removed from consideration, as such species are not going to be useful for OSC applications. This resulted in another 109425 species being removed from the CEPDB set, resulting in 2203603 remaining species to be used as potential training data.

After the CEPDB is pre-processed, stratified sampling is then applied to derive a set of 25000 candidate OSC donors for training and testing the machine learning models, as utilizing the full pre-processed CEPDB is computationally prohibitive. A set size of 25000 species is both computationally affordable and large enough for the training of machine learning models to be tractable, and is in line with previous literature works [49]. In this case, the maximum PCE value in the pre-processed CEPDB is 11.13%. As such, the pre-processed data are first assigned to 56 bins of equal widths of 0.2%, with the first bin including species with PCE [0,0.2) and the last bin including species with PCE [11.0,11.2). Once the pre-processed data is divided into the 56 bins, stratified sampling without replacement is then performed with respect to these bins. This is done so that the PCE profile of the selected 25000 species is close to the PCE profile for the entire pre-processed dataset. Once the 25000 species are selected, this is then divided into a set of 15000 species for training the machine learning method, a validation set of 5000 species used to evaluate the ML model fit while tuning hyperparameters, and a test set of 5000 species used to give the final evaluation of the ML model fit.

2.2 Harvard organic photovoltaic dataset

The second major dataset used in this work is the HOPV15 dataset, which consists of 350 different experimentally characterized organic solar cell donor structures that have been

collated from various works in the literature by Lopez et al. [22]. The HOPV15 data is accessible as a single file from the original publication [22]. For each of the 350 species, the HOPV15 data set contains the SMILES and InChI strings that define the molecular structure, as well as the DOI for the original work that experimentally characterized the species in question. The experimental data in HOPV15 also includes the construction type of the donor species, the architecture of the solar cell, the complement used (i.e. the acceptor material), and any measured photovoltaic characteristics of the organic solar cell. These photovoltaic characteristics include the HOMO and LUMO energies of the donor, the electrochemical and optical gaps of the donor, as well as the PCE, J_{sc}, V_{oc}, and Fill Factor, but not all of these properties are measured for all 350 species in HOPV15.

The HOPV15 dataset contains experimental results from a variety of different experimental conditions, which can be seen in the breakdown of the solar cell characteristics. There are 127 solar cells that made use of molecular constructions for the donor, whilst 220 used polymeric constructions for the donor species. In terms of the architecture, 270 experiments involved bulk heterojunction solar cells, 13 made use of bilayer solar cells for measurements, and 64 used Dye-Sensitized-Solar-Cells (DSSCs). The acceptor material used also varies, unlike in CEPDB. In this case 139 experiments made use of PC61BM as an acceptor, 133 used PC71BM, 9 used C60, 64 used TiO_2, 1 used ICBA, and 1 used PDI. For three species in the HOPV15, no experimental information was provided at all.

Given the variety of experiments used to generate the data in HOPV15, pre-processing and sampling are again applied to the data before any training and testing of machine learning algorithms is performed. As with CEPDB, the SMILES strings are first checked for validity. In this case, all 350 SMILES strings are able to be processed by RDKit. The second pre-processing step removes species that do not have experimental PCEs, which excludes 7 species. This leaves 343 species to be sampled from. It is worth noting that for these species, there is an extra atom type compared to CEPDB, namely that of fluorine, meaning 8 different atoms are possible. Additionally, whilst the smallest species in HOPV15 contains just 12 atoms, the largest contains 142 atoms, and the average size of species is roughly 71 atoms, meaning that in general the donor candidates here are much larger than the species in CEPDB. This, in addition with the extra atom type mean that HOPV15 contains substantially different structures for the ML methods to model when compared to CEPDB.

Although it is very affordable to train to the entirety of the HOPV15 data, as this involves just 343 PCE values and SMILES strings to be processed, there is the additional issue of the variability of experiments and solar cell set ups used to measure these PCEs. As a consequence, not all of the measured PCEs in HOPV15 are directly comparable as they are in the CEPDB, due to the differences in experimental methodology. Therefore, only PCEs measured using similar experimental conditions were selected to try and get a consistent dataset. Specifically, since the CEPDB PCE values assume a PCBM type material for the acceptor, PCEs measured with a solar cell that did not use PCBM or similar materials as the acceptor were excluded, namely those that used TiO_2. Similarly, only PCEs measured for solar cells using a bulk heterojunction architecture were chosen, to remove this variable from the dataset. This sampling meant that 267 PCEs were selected from the HOPV15 dataset to provide a more consistent set of experimental values to train the ML methods to.

It is worth noting that the HOPV15 data set also contains substantial computational data for each of the 350 organic solar cell donor candidates. This includes optimized geometries for up to 20 conformers for each species which are within 5 kcal/mol of the minimum energy structure at the BP86/def2-SVP level of theory [22]. Additionally, for each conformer, the HOMO, LUMO, HOMO-LUMO gap, J_{sc}, V_{oc}, and Scharber equation PCE are reported having been computed using the def2-SVP basis set and four DFT functionals, namely BP86, B3LYP, PBE0, and M06-2X. This does provide DFT data that could be incorporated as descriptors in the machine learning model. However, a sample comparison between the HOMO-LUMO gap, LUMO energy, and PCE predicted using B3LYP/def2-SVP and the corresponding experimentally measured values for these properties suggest poor agreement between computation and experiment. This is seen in Figure 1.

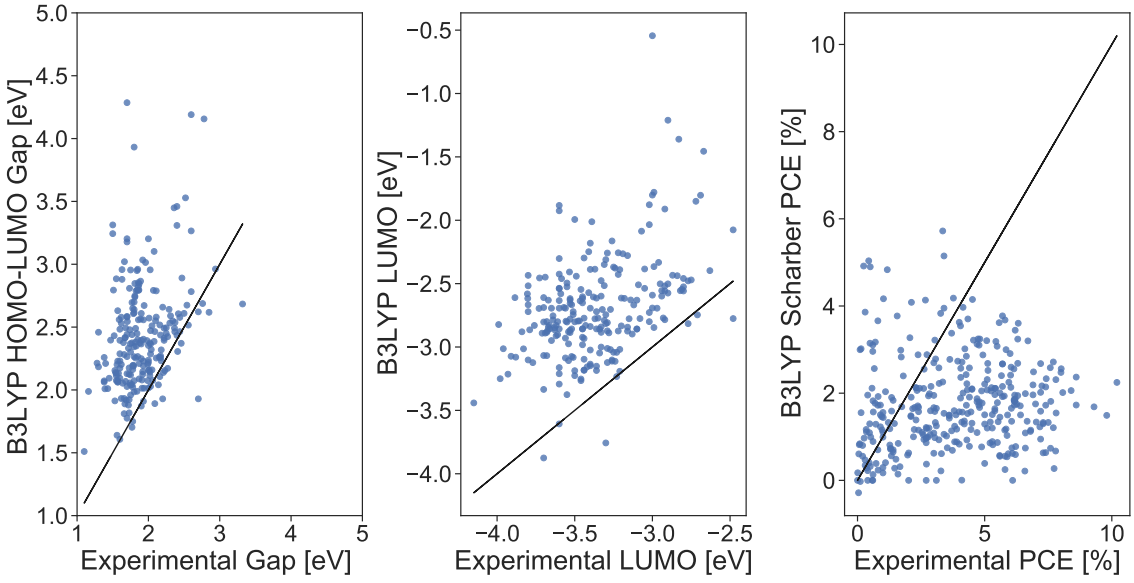

Figure 1: *Comparison between Donor Gap, Donor LUMO energy, and Scharber PCE predicted computationally by DFT and by various experiments in HOPV15.*

The agreement is also poor for the other three functionals used. This does suggest that PCEs purely predicted by the Scharber equation are insufficient to predict the actual performance of the material, in agreement with Padula et al. [27]. Furthermore, the plots also suggest that these popular DFT methods struggle when predicting the HOMO-LUMO gap and LUMO energy of the donor, two popular descriptors used for machine learning models of PCE. This may also explain why inclusion of properties computed by DFT in the previous work of Zhao et al. [54] resulted in only a modest improvement of the ML model performance, in that these properties are not well described by DFT and thus may not correlate well to experimental PCE results. Given this, it was decided that no additional descriptors predicted by DFT would be included in subsequent machine learning models, and that the models would only be trained to relate PCE to the underlying molecular structure of the donor as described by the SMILES strings.

3 Methodology

3.1 Models and descriptors

While the neural networks and ML methods utilized in this paper differ in many respects, they also have some general methodological steps in common. The steps common to all of the ML methods are introduced first, with details specific to each ML method introduced in the subsequent subsections. An overview of the structure of the ML methods utilized in this work is presented in Figure 2.

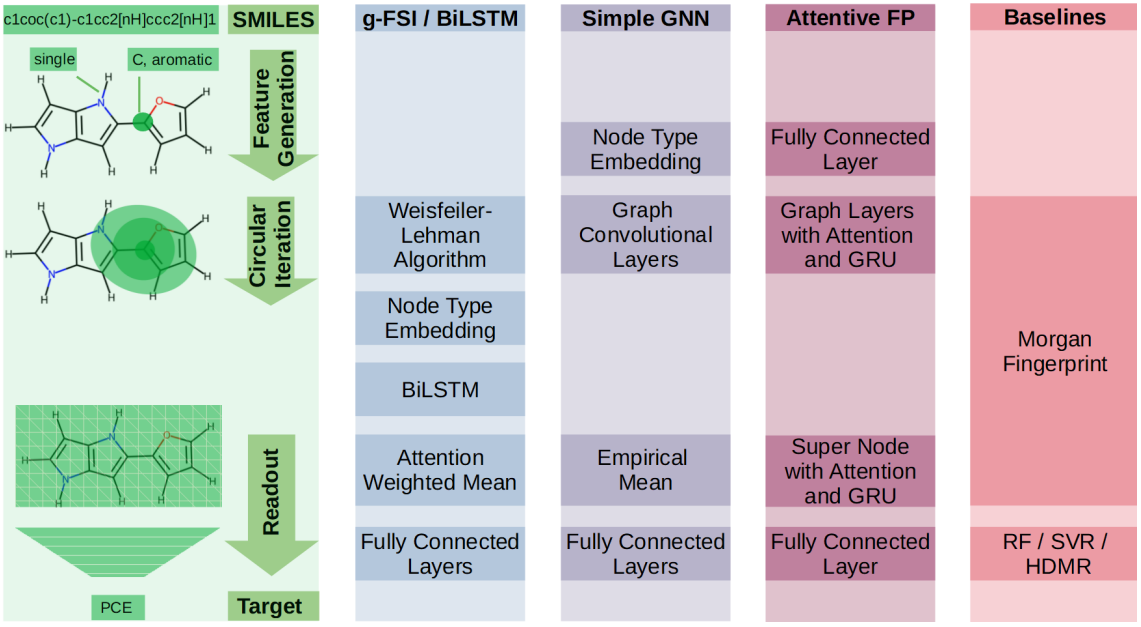

Figure 2: *Overview of neural networks and baselines used in this paper and alignment of their building blocks to three general steps: feature generation, circular iteration, and readout.*

The left-hand side of Figure 2 shows an example of a SMILES string and its corresponding structure for one of the smaller molecules in the CEPDB. This example structure contains only 21 atoms, including hydrogens, which are treated explicitly throughout this work. Figure 2 also illustrates three general methodological steps in the ML methods: feature generation, circular iteration, and readout. These are each discussed in turn below.

Feature generation. Feature generation is where a SMILES string is converted into a molecular graph. This graph represents the moleculuar structure, with node features including properties such as the atom type and aromaticity and edge features including properties like the bond type. These node and edge features are determined by RDKit [19].

Circular iteration. For a given node, circular iteration transforms and joins the features of this node with the features of its neighbour nodes and of the edges that connect them in a circular and iterative manner. An example is illustrated in Figure 2, for the carbon atom marked by a dark green dot. This carbon atom has three direct neighbour nodes with

atom types O, C and C which are connected by two aromatic bonds and one single bond. The green circle indicates the merge of the bond and neighbour features for the marked carbon atom in the first iteration. In parallel, the merge is performed analogously for each further node in the molecular graph and its direct neighbours. Afterwards, all node states are updated with the merged result. All ML methods perform these transformations and merging, but they do differ in the way of how they transform and merge the information.

Once one iteration is complete, the entire procedure may be repeated once again for the updated node states. After the second iteration, the updated node states now not only include information about the directly neighbouring nodes and connections, but also information about the direct neighbours' neighbours. For the carbon atom in Figure 2, this is indicated by the light green oval covering all nodes with a distance of one or two edges. As a consequence, as more merge and update iterations are performed, each node state will contain information on an increasingly large environment within the molecular graph.

Readout. First, all node states resulting from the previous circular iterations are aggregated to a single state on the graph level (i.e. on the molecule level). Next the aggregated state is used to predict the target value, e.g. by feeding it into a multilayer perceptron. The execution of these two steps comprises readout.

Note that some models in Figure 2 contain additional building blocks or steps that do not align perfectly with these three overarching steps. For instance, the BiLSTM is a central block in the g-FSI/BiLSTM model and is placed between the steps "Circular Iteration" and "Readout". Detailed descriptions of the steps that are specific to each ML method are provided in the following sections.

3.1.1 Bi-directional long short-term memory network

A sequential and deep-learning model using a bi-directional long short-term memory network with an attention mechanism and multilayer perceptron has been implemented. This architecture has been proven to be very successful for organic photovoltaics PCE prediction [49], thus it was decided to use it in this work as one of the neural models. Only the key model aspects are provided here. Readers are directed to [18, 49] for a more detailed description.

Feature generation. This step follows the common procedure as described previously. Atom types and their aromaticity are used to encode the node features whereas bond types (single, double, triple and aromatic bonds) are used to encode the edge features.

Circular iteration. The Weisfeiler-Lehman algorithm [47] is used to circulate around the nodes of molecular graphs generated in the previous step. The algorithm consists of two stages: (i) an initial assignment stage, in which each node and edge are assigned the unique integer identifiers that represent their starting features set, and (ii) an iterative updating stage, in which each node identifier is updated to reflect the identifiers of its neighbours and each edge identifier is updated to reflect the identifiers of nodes it connects. Once all nodes and edges have generated their new identifiers, the algorithm cycle is repeated until the requested number of iterations is reached. At the end, the final node identifiers are assembled into the final molecular fingerprint vector. Since the node and

edge features only include atom and bond types information, one can also think about this molecular fingerprint vector as a unique list of sub-molecular fragments building the parent molecule, hence the name graph fragments sequence identifiers (g-FSI) in the original publication [49]. In this paper only a single iteration of the Weisfeiler-Lehman algorithm has been performed by setting its radius parameter to one. To avoid the confusion with ordinary BiLSTM networks, the model will be referred to as g-FSI/BiLSTM for the remainder of the paper.

The g-FSI vector encodes two important structural aspects: fragment (fingerprint) types and their order in the molecule. Note that mapping discovered fragment types to unique integer identifiers proceeds on a first-found first-served basis with no hashing. Therefore, it is dependent on the order in which the data is processed. In order to eliminate this dependency, prior to using the model, the selected datasets are processed first to create the fragment-identifiers look-up dictionaries. This step also finds the molecules with the largest number of fragments which are in turn used to define the maximum sequence length for the BiLSTM network. Furthermore, it is important to highlight that the order of fragments in the g-FSI vector depends on the order in which the molecular graph nodes are processed. To keep the fragments that are spatially close to each other together (e.g two fragments that are part of the same aromatic ring), the molecular graph has been iterated in the breadth first search (BFS) order.

Node type embedding and BiLSTM. This step starts from passing the g-FSI vectors through a trainable embedding layer, which for a single molecule, results in creating a sequence of real-valued fragments embedding vectors (one for each fragment integer identifier). Secondly, the embedding vectors are processed by the forward and backward BiLSTM cells resulting in a sequence of hidden forward and backward state vectors.

Readout. In order to obtain the final PCE value, the two BiLSTM hidden states are concatenated and weighted-summed in the attention layer. This is followed by propagating the attention layer output through a multilayer perceptron.

3.1.2 Simple graph neural network

The neural network presented in this section is simple in three respects: (1) It belongs to the class of graph convolutional networks but is implemented in a straight-forward manner. Compared to [9] and [17] it simplifies the iteration update by applying the empirical mean. (2) Moreover, compared to g-FSI/BiLSTM model and Attentive FP, it does not make use of any attention mechanism. That means it treats all neighbours of all nodes in the same way. (3) It uses only a small number of node types as features and no edge features.

Feature generation. All distinguishable tuples of the form (atom type, atom aromaticity) are identified in the datasets leading to 8 and 12 different node types for CEPDB and HOPV15. This approach is equivalent to the Weisfeiler-Lehman algorithm for radius zero. Then, each different node type is mapped to its own vector in the space $\mathbb{R}^{\mathrm{ED}}$ where ED denotes the embedding dimension and the vector elements are trainable weights. While the

node types for Simple GNN are different from the fragment types for the g-FSI/BiLSTM model, their embedding into a continuous space is analogous.

Circular iteration. For each node v in the molecular graph, the embedding vector is chosen corresponding to its node type and used as initial node state $h^0(v) \in \mathbb{R}^{\mathrm{ED}}$. The graph layers of simple GNN are indexed with l ranging from 1 to the overall layer count, CL. Each layer can be described in terms of the message passing neural network (MPNN) framework introduced in [10]: First, messages with transformed states are received from v's direct neighbour nodes $N(v)$ and aggregated,

$$m^l(v) = \frac{1}{\#N(v)} \sum_{u \in N(v)} W^l h^{l-1}(u) \tag{4}$$

where $W^l \in \mathbb{R}^{\mathrm{ED} \times \mathrm{ED}}$ denotes a matrix of trainable weights and $\#N(v)$ is the number of neighbour nodes. Finally, the state of node v at layer l is updated by

$$h^l(v) = \mathrm{relu}(h^{l-1}(v) + m^l(v)) \tag{5}$$

where the rectified linear activation function, relu, is applied component-wise. For simplicity, W^l is a square matrix such that all node states have the same dimension, ED, throughout all graph layers. Here, the layer count, CL, plays the same role as for Attentive FP (section 3.1.3), as the radius in the Weisfeiler-Lehman algorithm (section 3.1.1), and as the radius for generating Morgan fingerprints (see section 3.1.4): it corresponds to the maximum distance of (direct and indirect) neighbour nodes that may contribute to the final state of node v.

Readout. The state of the graph G is set to the empirical mean over all node states at layer $l = \mathrm{CL}$, i.e.

$$h(G) = \frac{1}{\#N(G)} \sum_{u \in N(G)} h^{\mathrm{CL}}(u) \tag{6}$$

where $N(G)$ is the set of all nodes in G. Finally, the graph state $h(G) \in \mathbb{R}^{\mathrm{ED}}$ is fed into a multilayer perceptron with one output neuron for PCE prediction analogously to the g-FSI/BiLSTM model from section 3.1.1.

3.1.3 Attentive fingerprint

Attentive FP (fingerprint) is a graph neural network that was introduced by Xiong et al. [52] and achieves state-of-the-art performance on several data sets that are widely used in ML research according to a comprehensive assessment of several neural networks and ML methods by Wu et al. [50]. Attentive FP makes use both of Gated Recurrent Units (GRU, [7]) and attention and thus resumes ideas of Gated Graph Neural Networks [21] and Graph Attention Networks [45]. It applies the attention mechanism both on the atomic node level and on the molecular graph level to focus on substructures that are relevant for

predicting target variables.

Feature generation. Nine node features (including atom types and atom aromaticity) and four edge features (including bond type) are used as input features, with most of them being one-hot encoded. A detailed list of the input features can be found in Xiong et al. [52].

Circular iteration. For each target node v in the molecular graph, its node features are fed into a fully connected layer with FS units where FS denotes the Fingerprint Size. The output is used as initial node state $h^0(v) \in \mathbb{R}^{\mathrm{FS}}$. Edge features are handled explicitly only at the beginning of the first iteration: the node features of each direct neighbour $u \in N(v)$ and the features of the edge between u and v are concatenated and fed into another fully connected layer having the same number FS of units. From here, all states have the same size FS and the actual circular iteration can be formulated in terms of the MPNN framework [10] - analogously to the simple GNN from the previous section. Roughly speaking, all summands in Equation 4 are multiplied with their corresponding attention weights calculated between the states of v and u and replacing the uniform weights $\frac{1}{\#N(v)}$. Then, their sum is fed as input vector into a GRU which replaces the simple update function in Equation 5. This means the state of v is updated to the resulting hidden state of the GRU at the end of each iteration and is used as the starting point for the next iteration.

Readout. A virtual super node is added to the molecular graph and connected to all of its atom nodes. Its state represents the state of the entire graph and is initialized with the sum of all atom node states updated at the end of the last iteration. The super node state itself is updated throughout several iterations using its own GRU. In each iteration, the attention weight between the super node and an atom node is calculated in the same way as between two atom nodes. Finally, the super node state is fed into a fully connected layer which has one output neuron in the case of PCE as target variable.

The GRU can be regarded as a less complex version of an LSTM. The g-FSI/BiLSTM model uses breadth first search for ordering the fragments of a molecule and applies two LSTMs in a bidirectional manner to find patterns within the "horizontal" sequence of ordered fragments. In contrast, the GRU in Attentive FP conveys information for each target node in the molecular graph "vertically", i.e. from layer to layer, and in each layer, the local environment from its direct neighbours is merged with its own information from previous layers (i.e. from previous time steps). Moreover, the information flows for all nodes layer-wise and in parallel and the nodes share the same GRU and corresponding trainable weights.

3.1.4 Baseline models

In this paper, we use Morgan fingerprints as input features for all baseline methods. The main idea behind Morgan fingerprints stems from the Morgan algorithm [25] which aims to provide a unique numbering scheme of chemical structures. The Morgan algorithm is specific to molecular graphs and tries to solve the isomorphism problem between them, while the Weisfeiler-Lehman algorithm shares the same goal for graphs in general.

RDKit implements Morgan fingerprints along the Extended Connectivity Fingerprint algorithm, a modified Morgan algorithm described in [32]. The generation of Morgan fingerprints requires two integer-valued parameters - the fingerprint radius, FR, and the fingerprint size, FS, - and involves several steps as illustrated in Figure 2. This includes applying the three general steps of feature generation, circular iteration, and readout as follows:

Feature Generation. RDKit converts SMILES into molecular graphs with atom and bond features and uses these features to generate the corresponding Morgan fingerprints.

Circular iteration. For each atom in the molecular graph, an identifier is initialized as a bit vector derived from the atom features. In a predefined order, each identifier is concatenated with the identifiers attached to its direct neighbour atoms and with the bit-encoded types of bonds in between. Then, a suitable hash function is applied to the concatenated bit vector to obtain a vector that has a fixed length (usually, 32 or 64 bits) and differs from other generated bit vectors with high probability. Finally, all atom identifiers are updated with the hashed vectors and the entire procedure is repeated until the maximum number of iterations - given by the radius FR - is reached.

Duplicate Structure Removal. All atom identifiers during initialization and all iterations are gathered. In this additional removal step, identifiers referring to the same substructure are removed.

Readout. A fingerprint vector with FS bits is initialized with zeros. Each remaining identifier is converted to an integer i and the bit at position $(i \mod \mathrm{FS})$ in the fingerprint vector is set to one.

The resulting bit vector is called a Morgan fingerprint. If the hash function is chosen properly and FS is large enough, collisions are unlikely and consequently, different substructures tend to be represented by different bits. While Figure 2 emphasizes the iterative behaviour that the fingerprint algorithm has in common with the Weisfeiler-Lehmann algorithm and graph neural networks, Morgan fingerprints are usually regarded as part of the feature generation. Next, we will shortly describe the baseline methods and how they make use of Morgan fingerprints as input features.

Support Vector Regression (SVR)

The support vector regression model uses the support vector machines for function estimation [39]. Two important hyperparameters are the regularization parameter C and the parameter ε, which specifies that the loss between the predicted value and the target value vanishes if their distance is smaller than ε. As in [54], we use the RBF kernel and replace the metric term between two points in the Euclidean space by a distance term between two Morgan fingerprints. The resulting function is:

$$\exp(\mathrm{GK}(1 - T(x,x'))^2) \tag{7}$$

where the kernel coefficient GK is a hyperparameter, x and x' are two bit vectors of size FS and T denotes the Tanimoto similarity index given by

$$T(x,x') = \frac{\sum_{1\leq i\leq \mathrm{FS}}(x_i \wedge x'_i)}{\sum_{1\leq i\leq \mathrm{FS}}(x_i \vee x'_i)} \in [0,1] \tag{8}$$

Random forests (RF)

Random forests (RF) is an ensemble method that can be used for classification and regression. The method constructs a number of decision trees by randomly subsampling from the dataset and by randomly selecting subsets of features [6]. The method makes a prediction by averaging the outcome of the decision trees. Important hyperparameters are the number of trees, the maximum number of samples and the maximum number of features. A full list of the RF hyperparameters and their ranges is provided in Table A2 in the Appendix. In the case of Morgan fingerprints, the fingerprint size corresponds to the number of overall features from which a maximum number of bits is selected for constructing an individual decision tree.

High Dimensional Model Representation (HDMR)

The High Dimensional Model Representation is the final chosen baseline model. The method works by approximating an unknown multivariable function, f, using its finite expansion [31]. In this case, f represents a mapping between a molecular fingerprint vector bit values, x_i and the final power conversion efficiency of an organic heterojunction solar cell, y, with the molecular fingerprint vector generated from the structure of the donor candidate molecule. Under the HDMR representation, the function, f can be approximated using the following expression:

$$y \approx f(x) = f_0 + \sum_{i=1}^{N_x} f_i(x_i) + \sum_{i=1}^{N_x}\sum_{j=1}^{N_x} f_{ij}(x_i,x_j), \tag{9}$$

where N_x is the dimension of the input space, for this application it is equal to the fingerprint size, FS, and f_0 represents the mean value of $f(x)$. The above approximation is sufficient in many situations in practice since terms containing functions of more than two input parameters can often be ignored due to their negligible contributions compared to the lower-order terms [20]. The terms in Equation (9) are evaluated by approximating the functions $f_i(x_i)$ and $f_{ij}(x_i,x_j)$ with orthonormal basis functions, $\phi_k(x_i)$. In this work, the basis functions have been constructed from ordinary polynomials [20]. The HDMR parameters are listed in Table A2.

3.2 Training and hyperparameter optimisation

Given the complexity and the number of different machine learning models considered in this work, performing manual hyperparameter fine-tuning for all of the models would present a substantial challenge. Furthermore, if each model has manual fine-tuning of its hyperparameters, it becomes difficult to create a fair comparison between models, as one may have just had its hyperparameters tuned more carefully than another. Instead, two different automated strategies have been used to try and keep a level of consistency in how the different models have their hyperparameters tuned. These strategies are explained below.

Strategy I. This strategy is depicted in Figure 3 and has been used for hyperparameter optimisation when training each ML method on the CEPDB dataset. The dataset is split into three sets: training, validation and test sets with a ratio of 0.6/0.2/0.2. Then a Bayesian optimisation based hyperparameter tuning is performed where the models are trained on the training set with different configurations (trials) sampled within the search space. In case of the neural models (g-FSI/BiLSTM, Simple GNN and Attentive FP) the training process is performed for 400 epochs using the Adam optimiser [16]. The validation set is used to monitor the training process using the mean squared error as the performance metric. For the neural models, this metric was employed for early stopping to prevent over-fitting, as well as assessing the performance of suggested parameter configurations. For all models aside from HDMR, 10 trials are first randomly sampled for the hyperparameter optimiser to estimate a statistical model for the objective function. The remaining 90 trials are suggested by an acquisition function that is continuously updated over the performance of the sampled combination of hyperparameters. The whole process is handled by the Tree-structured Parzen Estimator algorithm implemented in the Optuna framework.

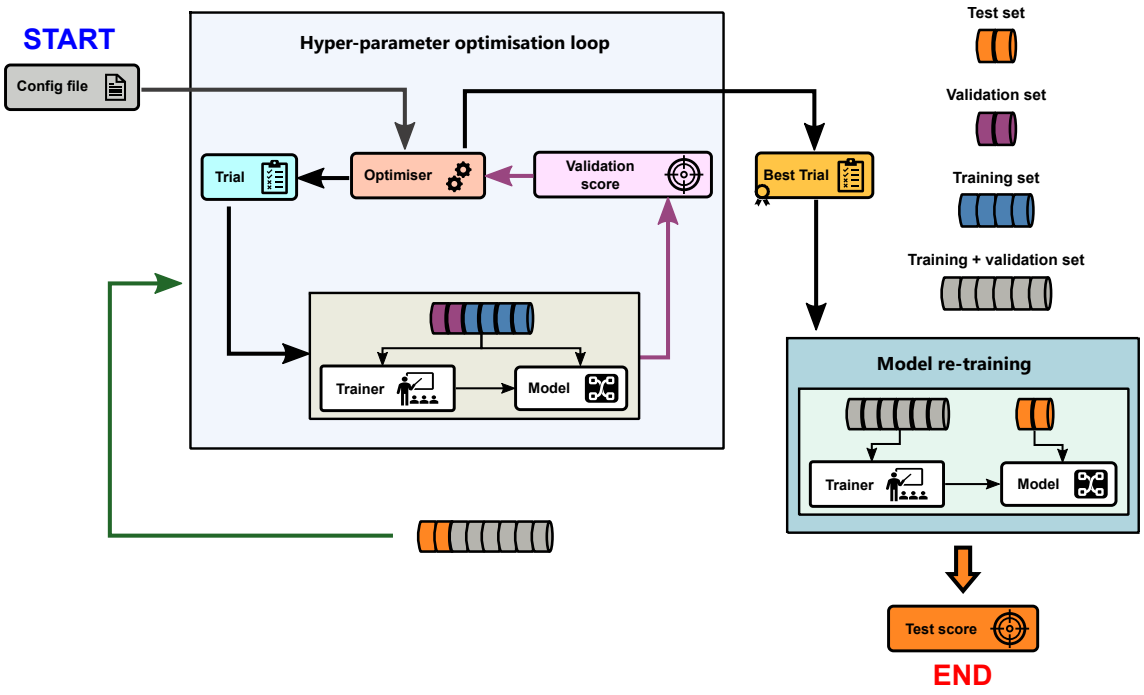

Figure 3: *Strategy I: hyperparameter optimisation and model re-training.*

In case of the HDMR model, since the only considered hyperparameters are 6 different fingerprints bit numbers and 4 different radii (as shown in Table A2), it was possible to do a full manual grid-search approach, resulting in 24 trials performed. Subsequently, the hyperparameters of the best trial are used in the final model-retraining step. The training and validation sets are combined and re-shuffled with a different seed for the new split. Each model was again trained with early stopping monitored. The final model performance is checked on the test set, which is withheld from the machine learning method throughout

the hyperparameter optimisation process.

Strategy II. This strategy is depicted in Figure 4 and has been used to fine-tune the ML models on the HOPV15 dataset. It can be seen that strategy II differs from strategy I only by the additional use of nested cross-validation. In this approach, the hyperparameter optimisation and the model generalisation error estimation are performed m times by separating m different test and training sets from the whole dataset. This is also called the outer loop. Then, for each m-fold dataset split, the training set is further split into k different training and validation sets, which constitutes an inner loop. Subsequently, for the same set of hyperparameters suggested by the optimiser, k different models are trained, each using a different k-fold split of the total training data. Then, the mean squared validation error across all the trained models is used to assess the final trial performance. In the end, m best trials are found and tested in the model re-training step. The final model test score is taken as the mean squared test error across all m folds. Given that the HOPV15 dataset size is not too prohibitive, the total number of outer and inner folds, (m, k), was set to 5 for all of the models. The remaining details of the model training and trial sampling procedures are the same as in the strategy I.

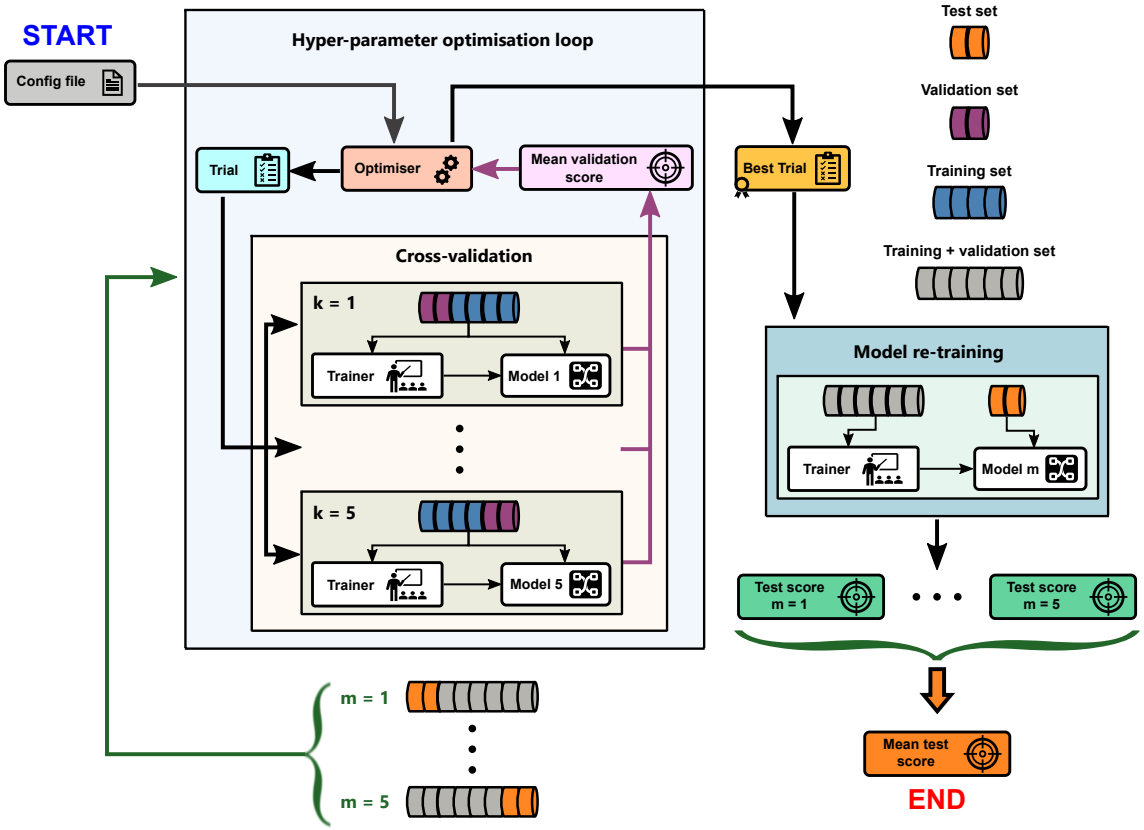

Figure 4: *Strategy II: hyperparameter optimisation and model re-training.*

Further information regarding the choice of hyperparameters set for each model and their sampling ranges can be found in the Appendix A.

3.3 Software and tools

All of the machine learning models considered in this work, except the HDMR, were implemented in Python. The g-FSI/BiLSTM model was re-implemented using the PyTorch framework and by following the original description of the model in Wu et al. [49]. The PyTorch backend of the Deep Graph Library (DGL) [46], was used to build the Simple GNN model. For Attentive FP, the code was obtained from a publicly available repository [1]. The RF and SVR baseline models were built in Python using the Scikit learn library [28], whereas all the HDMR simulations were performed using a commercial software, Model Development Suite (MoDS) [8]. The conversion of SMILES strings to molecular graphs as well as molecular fingerpint generation were done using the RDKit library [2]. Finally, the hyperparameter optimisations were performed with Optuna [4] for all models aside from HDMR.

4 Results and discussion

4.1 Harvard clean energy project dataset results

This section presents the results obtained by optimising and training the selected ML models on the CEPDB dataset using strategy I. The final models performance metrics for predicting power conversion efficiencies of organic solar cells, in terms of mean squared error (MSE), mean absolute error (MAE), coefficient of determination (R^2) and Pearson correlation coefficient (r), are collated in Table 1.

Table 1: *Performance of the models trained on CEPDB data in predicting the PCE values of organic photovoltaics.*

Model / Dataset	CEPDB				
	set	MSE	MAE	R^2	r
g-FSI/BiLSTM	train	0.038	0.151	0.993	0.997
	val	0.207	0.322	0.964	0.982
	test	0.225	0.329	0.961	0.981
Simple GNN	train	0.036	0.145	0.994	0.997
	val	0.085	0.208	0.985	0.993
	test	0.091	0.209	0.984	0.992
Attentive FP	train	0.024	0.118	0.996	0.998
	val	0.062	0.176	0.989	0.995
	test	0.071	0.180	0.988	0.994
SVR	train	0.008	0.009	0.999	0.999
	test	0.297	0.383	0.949	0.974
RF	train	0.008	0.060	0.999	0.999

Table 1: *(Continued)*

	test	0.569	0.534	0.902	0.950
HDMR	train	0.413	0.475	0.929	0.964
	test	0.530	0.536	0.909	0.953

The results in Table 1 suggest that all models can achieve a reasonably good fit for the CEPDB data, with the largest test set MSE being 0.569 for random forests. However, there are still some differences between the performance of the ML methods, and so each method is discussed in turn.

g-FSI/BiLSTM. Although this model still performs rather well with a quite low test set MSE of 0.225, it performs relatively poorly when compared to the other neural models. By comparing the training and validation sets errors, it can be inferred that there is some degree of over-fitting. As mentioned in section 3.1.1, this ML architecture has been applied previously to the CEPDB dataset by Wu et al. [49] who managed to obtain the test set MSE of 0.12. Although this is lower than the current results, it is important to understand that the sampled CEPDB data points used in this and Wu et al. [49] studies were not the same, hence difference in performance.

Attentive FP. This model performs the best out of all the ML methods, with the MSE as low as 0.071 on the test set. This is, to the best of our knowledge, the best result obtained so far on the CEPDB dataset. The next best result is from our Simple GNN model (explained in the next paragraph), whereas the next best literature result of 0.12 MSE is from Wu et al. [49] as explained previously. Figure 5 visualises the predicted vs measured PCEs for the training and test sets, where only a little scatter is observed. Xiong et al. [52] evaluated their Attentive FP on several data sets ranging from quantum chemistry to physiology and achieved state-of-the-art predictive performance. They also trained their model on a CEPDB subset and reported a mean MSE of 0.82 ± 0.07 which was calculated from three runs for different seeds using optimized hyperparameter values. As described in section 2.1, species with a PCE value smaller than 0.0001 were removed from CEPDB during pre-processing. Without the removal of these species, the implementation for Attentive FP used in this work yields an error of the same order, suggesting the results are consistent with Xiong et al. [52].

Simple GNN. The model has been found to have the second best performance with the test set MSE of 0.091. This is somewhat surprising, given the simplicity of the method and the fact that it uses only two atom features. This demonstrates the power of graph neural networks, and how they are a rather natural machine learning approach to modelling molecules.

The optimal hyperparameters derived for each neural method are collated in Table A3 in the Appendix. It can be seen that the g-FSI/BiLSTM and Simple GNN methods have the same optimal embedding dimension and number of MLP hidden layers. The optimal number of neurons in the hidden layer is also nearly the same for these two methods.

Baseline models. The three selected baseline models have shown to offer a robust alterna-

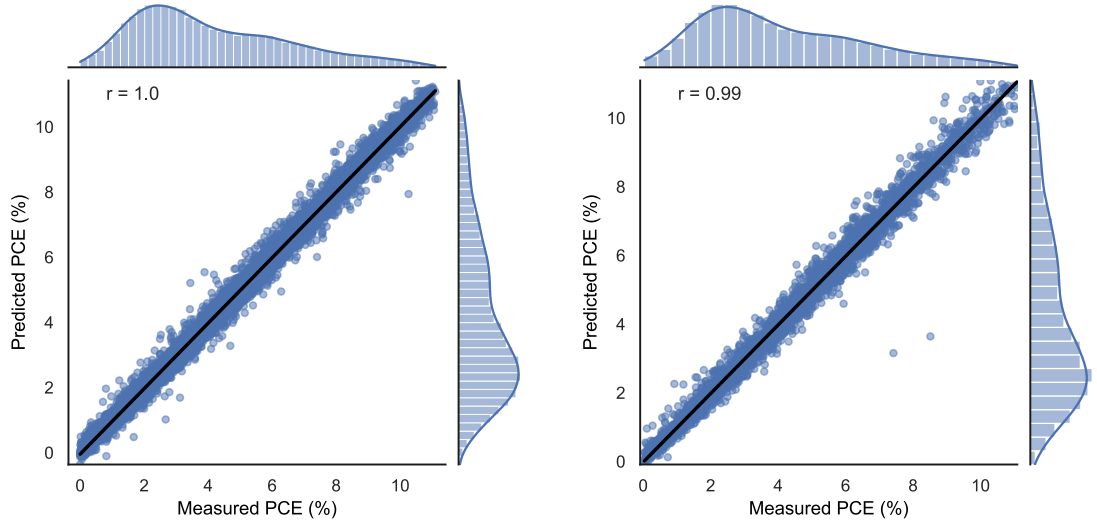

(a) Training set

(b) Test set

Figure 5: *Attentive FP regression plot showing the predicted vs measured PCEs for the training (a) and test (b) sets. The marginal distribution of the measured and predicted PCE values are plotted at the side and on the top.*

tive to their neural models counterparts. Support vector regression is the best performing baseline model with a test set MSE of 0.297. Figure 6 shows the predicted vs measured PCEs for the training and test sets. It can be seen that these plots have a bit more scatter in them when compared to the same plots for Attentive FP.

It can also be noticed from Table 1 that HDMR and random forests have comparable performance with their test set MSEs of 0.530 and 0.569 respectively. This is rather surprising for HDMR, as the model is not naturally suited to deal with integer-valued inputs, making this particular application a rather challenging one.

Table A4 in the Appendix lists the most optimal hyperparameters for all of the baseline models. Noticeably, the optimal fingerprint size and radius is same across all three models. This does mean that there is some generality as to which parameters are suitable for the CEPDB dataset for both the neural and baseline ML methods.

4.2 Harvard organic photovoltaic dataset results

This section presents the results obtained by optimising and training the selected ML models on the HOPV15 dataset using strategy II. Table 2 collates the mean performance metrics for all the models across all 5 outer loop cross-validation folds. The error bar estimates are also provided and are given as one population standard deviation, which for a normal distribution would correspond to a 68% confidence interval.

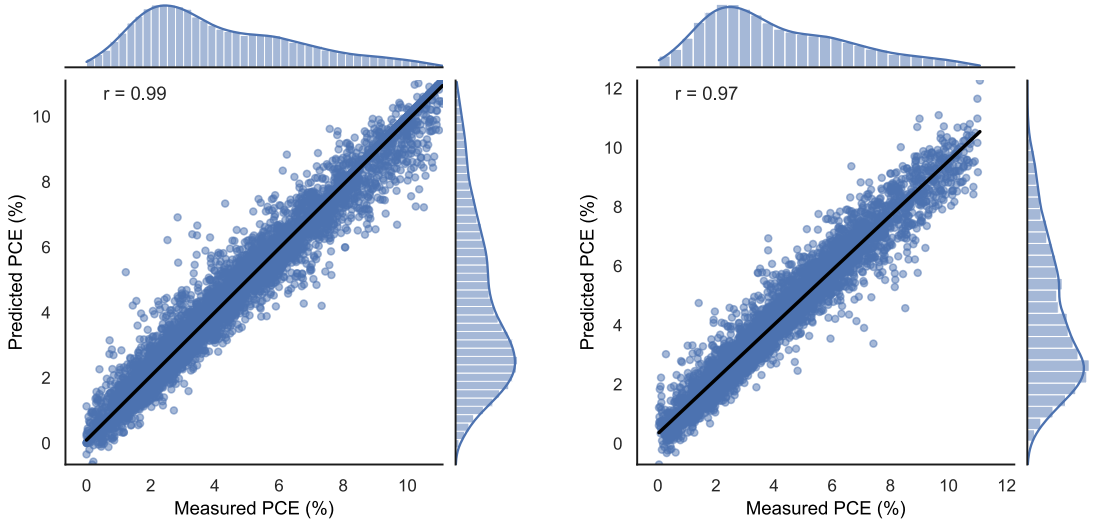

(a) Training set (b) Test set

Figure 6: *Support vector regression plot showing predicted vs measured PCEs for the training (a) and test (b) sets. The marginal distribution of the measured and predicted PCE values are plotted at the side and on the top.*

Table 2: *Performance of the models trained on HOPV15 data in predicting the PCE values of organic photovoltaics.*[a]

Model / Dataset		HOPV15			
	set	$\overline{\text{MSE}}$	$\overline{\text{MAE}}$	$\overline{\text{R}^2}$	$\bar{\text{r}}$
g-FSI/BiLSTM	train	1.072 ± 0.675	0.780 ± 0.271	0.776 ± 0.149	0.900 ± 0.079
	val	3.273 ± 0.447	1.425 ± 0.141	0.363 ± 0.067	0.625 ± 0.052
	test	3.486 ± 0.647	1.480 ± 0.169	0.299 ± 0.090	0.580 ± 0.064
Simple GNN	train	1.494 ± 0.712	0.918 ± 0.300	0.711 ± 0.128	0.866 ± 0.065
	val	2.641 ± 0.695	1.293 ± 0.166	0.426 ± 0.073	0.680 ± 0.063
	test	3.295 ± 0.279	1.454 ± 0.092	0.330 ± 0.053	0.598 ± 0.047
Attentive FP	train	2.936 ± 1.101	1.377 ± 0.377	0.420 ± 0.211	0.648 ± 0.138
	val	3.020 ± 0.964	1.397 ± 0.227	0.355 ± 0.081	0.597 ± 0.070
	test	4.417 ± 1.503	1.672 ± 0.223	0.127 ± 0.193	0.455 ± 0.113
SVR	train	0.276 ± 0.479	0.196 ± 0.306	0.946 ± 0.093	0.973 ± 0.046
	test	2.687 ± 0.487	1.319 ± 0.095	0.453 ± 0.109	0.684 ± 0.083
RF	train	0.703 ± 0.610	0.579 ± 0.343	0.859 ± 0.123	0.934 ± 0.059
	test	2.876 ± 0.415	1.318 ± 0.065	0.414 ± 0.089	0.657 ± 0.061
HDMR	train	0.724 ± 0.171	0.673 ± 0.070	0.855 ± 0.035	0.927 ± 0.019

Table 2: *(Continued)*

	test	3.185 ± 0.540	1.411 ± 0.080	0.350 ± 0.135	0.623 ± 0.078

[a] Provided model accuracy metrics are given as a mean across all m-folds and the error bars are given as σ, which for a normal distribution would correspond to a confidence level of 68%

g-FSI/BiLSTM. The model mean test MSE is second lowest of the neural models. Nevertheless, the model performance is much worse compared with the CEPDB dataset. The obtained mean test MAE of 1.480 is a bit higher than the value reported by Wu et al. [49], where it was about 1.25 (without cross-validation).

Attentive FP. This model now has the worst performance across all the tried models with a mean test MSE of 4.417. The model also has the largest variation across the outer cross-validation folds, meaning it is very sensitive to the partition of the training set. This is in complete contrast to its performance on the CEPDB dataset, when it was found to be the best performer. A potential explanation for these "surprising" findings could be that among all of the ML models, Attentive FP is the most sophisticated one. Therefore, the small and varied amount of data in the HOPV15 dataset might make it difficult to train.

Simple GNN. Although the model has the best test MSE and MAE among all the tried neural models and one of the lowest variations across outer cross-validation folds, its performance on HOPV15 is still much worse compared to CEPDB.

Baseline models. In case of the HOPV15 dataset, the three baseline models perform much better than their neural counterparts. This time, SVR is not only the best performing baseline model with respect to the test MSE, as it was on the CEPDB dataset, but it is also the best performing overall model. The second best performing model is RF with the test set MSE of 2.876 followed by the HDMR model with 3.185 MSE. However, the mean test errors for SVR, RF and HDMR only slighty differ, in particular when considering their relatively large empirical variance. Nevertheless, the baseline model results confirm the known fact that when training to smaller datasets with larger variability, it can be advantageous to have fewer degrees of freedom in the models.

As the models generally performed poorly on the HOPV15 dataset, the potential of transfer learning to improve model performance was also assessed. Transfer learning was implemented for all three neural network models by taking the best model identified during the hyperparameter optimisation on CEPDB dataset and continually training on the HOPV15 dataset in an end-to-end fashion. The rationale is that the neural network models are believed to be able to generalise the fragments and sub-structures of a molecule that are important to PCE when trained on the CEPDB, thus accelerating the learning process when the model is applied to a smaller but somewhat different dataset like HOPV15. The model performance when utilizing transfer learning was compared to the model performance when the weights are randomly initialized and trained on the HOPV15 dataset. However, the transfer learning did not result in any statistically significant improvement in performance.

Analysing the results it can be seen that for HOPV15 dataset the selected machine learning models are all unable to present a clear correlation between the molecular structures from SMILES and the target PCE which was not the case for the CEPDB dataset. It is then important to discuss potential causes of such a poor models behaviour on HOPV15. One, rather obvious, reason is that the HOPV15 data are inhomogeneous, meaning that they were collated across different labs, so it is very unlikely that the data points are from the same experimental setups. As a consequence, the PCEs are much more difficult to compare, as they are not all determined using the same method like is done computationally with the CEPDB. Different experiments also have different associated errors with them, which have not been included or taken into consideration here. Furthermore, there is an extra atom type included in the HOPV15 that is not in the CEPDB, which is fluorine. The number of fragment types in HOPV15 is also much larger in comparison to CEPDB, with HOPV15 having 156 fragments in comparison to just 56 in CEPDB. This means that the chemical complexity of HOPV15 is higher than CEPDB, which poses a challenge as the dataset is much smaller to begin with. Additionally, the number of variables influencing PCE in the real-world OPV materials is likely larger compared to the number of variables in the simple Scharber model (CEPDB dataset). While some of these variables may correlate with structural information encoded in SMILES strings, it is plausible that there are other non-accounted for factors. For example, this includes bulk properties of OPV materials such as the structure of the layer and OPV itself, the microstructure of any polymers used in the OPV conjunction, and the contact area between the donor and acceptor in the OPV to name a few [44]. These factors likely make the HOPV15 dataset more challenging for machine learning purposes.

5 Conclusions

In this paper, the ability of five machine learning models and HDMR to predict the PCE of organic photovoltaics based on molecular structure information is assessed, including the impact and implications of the choice of training data. Three neural (gFSI/BiLSTM, Simple GNN and Attentive FP) and three baseline (SVR, RF, HDMR) models are trained on the larger, computational Harvard CEPDB dataset and on the much smaller, experimental HOPV15 dataset.

The contrasting datasets result in contrasting performance of the machine learning models. In the case of the CEPDB, the Simple GNN and Attentive FP neural models work very well, and the Attentive FP in particular achieves very low test MSE. The g-FSI/BiLSTM performs noticeably worse. The baseline models perform worse on average than the neural models, although SVR does reasonably well. In general, all the machine learning models are able to derive high correlation coefficients between the learned PCE values and the actual PCE values in the CEPDB, suggesting that the CEPDB PCE values correlate well to the SMILES string of the donor molecules.

In the case of the HOPV15, the performance of all machine learning models is much worse. Attentive FP now performs the worst, with Simple GNN and g-FSI/BiLSTM also

presenting very large errors. Contrary to the CEPDB, the baseline models now outperform the neural methods, which could due to the fact that the neural methods need to train the weights and have insufficient data to do so. Still, the performance of all machine learning models is not very good. This is likely due to the nature of the HOPV15 dataset, which is smaller and also much less homogeneous than CEPDB due to expected differences in experimental set ups, larger chemical complexity of the species in the dataset, and possibly a larger number of variables influencing real-world organic solar cell PCEs that may not be strongly correlated with the structural information of the donor molecules encoded in the SMILES strings, such as bulk solar cell properties. Transfer learning was also tried for the neural models by first training on CEPDB and then training on the HOPV15 dataset. The transfer learning did not result in any statistically significant changes in performance, which is possibly due to the aforementioned differences between the two datasets.

Ultimately, whilst a variety of machine learning methods can accurately model PCEs predicted by the Scharber Model and DFT, they struggle with modelling experimentally determined PCEs. This is an issue as the computed PCEs do not match well with experimentally determined PCEs. Going forward, to improve the performance of ML models in predicting PCEs that agree with experimental methods, more experimental measurements at a consistent set of experimental conditions would be useful. Alternatively, trying to improve the computational results so that they are more in line with experimental measurements, either by making use of more accurate quantum chemical calculations, or better methods for estimating the PCE, may also help, as these are much easier to standardize and a large amount of starting data that can be improved upon already exists. This will hopefully improve the potential of fast, computational screening of candidate organic photovoltaic donors for clean energy generation in the future.

Acknowledgements

This research is supported by the National Research Foundation, Prime Minister's Office, Singapore under its Campus for Research Excellence and Technological Enterprise (CREATE) programme. J. Bai acknowledges financial support provided by CSC Cambridge International Scholarship from Cambridge Trust and China Scholarship Council. MK gratefully acknowledges the support of the Alexander von Humboldt foundation.

A Appendix

Table A1: *Neural models hyperparameters.*

Parameter name	Parameter value	Parameter sampling
	g-FSI/BiLSTM	
Max sequence length (SEQ)	60, 160	fixed value[a]
No. of attention neurons (NA)	SEQ	fixed value
Embedding dimension (ED)	8, 16, 32, 64, 128, 256	categorical
No. of neurons in MLP input layer (NI)	$2 \times$ ED	fixed value
No. of hidden MLP layers (NL)	1 – 4	integer
No. of hidden MLP neurons (HN)	8 – 256	custom-integer[b]
Dropout rate (DR)	$0.0 - 0.3$	uniform
Learning rate (LR)	$10^{-5} - 10^{-2}$	log-uniform
Weight decay rate (WD)	$10^{-5} - 10^{-2}$	log-uniform
	Simple graph neural network	
Embedding dimension (ED)	8, 16, 32, 64, 128, 256	categorical
No. of convolutional layers (CL)	1 – 6	integer
No. of hidden MLP layers (NL)	1 – 4	integer
No. of hidden MLP neurons (HN)	8 – 256	custom-integer[b]
Dropout rate (DR)	$0.0 - 0.3$	uniform
Learning rate (LR)	$10^{-5} - 10^{-2}$	log-uniform
Weight decay rate (WD)	$10^{-5} - 10^{-2}$	log-uniform
	Attentive fingerprint	
Fingerprint size (FS)	8 – 256	integer
No. of atom node layers (AL)	1 – 6	integer
No. of super node layers (SL)	1 – 4	integer
Dropout rate (DR)	$0.0 - 0.3$	uniform
Learning rate (LR)	$10^{-5} - 10^{-2}$	log-uniform
Weight decay rate (WD)	$10^{-5} - 10^{-2}$	log-uniform

[a] first value - CEPDB, second value - HOPV15

[b] the number of neurons in the first hidden layer is fixed and equal to the size of the embedding dimension: $\mathrm{HN}_1 = \mathrm{ED}$; the number of neurons in the subsequent layers is sampled from the provided range in decreasing direction (is equal to or smaller than the number of neurons in the previous layer): $\mathrm{HN}_i \leq \mathrm{HN}_{i-1} \quad i = 2,3,4$

Table A2: *Baseline models hyperparameters.*

Parameter name	Parameter value	Parameter sampling
	Fingerprint parameters (all baseline models)	
Fingerprint size (FS)	128, 256, 512, 1024, 2048, 4096	categorical
Fingerprint radius (FR)	2, 3, 4, 5	categorical
Fingerprint chirality (FC)	True	fixed value
Fingerprint bond types (FB)	True	fixed value
	Support vector regression parameters	
SVR kernel (SK)	custom-rbf	-
Gamma kernel coefficient (GK)	10^{-3} – 20.0	loguniform
Regularization parameter (CP)	10^{-1} – 20.0	loguniform
Epsilon parameter (EP)	10^{-4} – 1.0	loguniform
	Random forests parameters	
No. of trees (NT)	16 – 256	integer
Max tree depth (MD)	10 – 100	integer
Min samples split (MSS)	2 – 5	integer
Min samples leaf (MSL)	1 – 5	integer
Max features (MF)	0.05, 0.1, 0.5, 1.0	categorical
Bootstrap (BS)	True, False	categorical
Max samples (MS)	5 – 50	integer
	High dimensional model representation parameters	
Polynomial order (PO)	6	fixed value
HDMR order (HO)	2	fixed value

Table A3: *Neural models optimal hyperparameters for CEPDB dataset after 100 trials.*

Parameter name	Optimal parameter value
g-FSI/BiLSTM	
Max sequence length (SEQ)[a]	60, 160
No. of attention neurons (NA)	SEQ
Embedding dimension (ED)	256
No. of neurons in MLP input layer (NI)	$2 \times$ ED
No. of hidden MLP layers (NL)	1
No. of hidden MLP neurons (HN)	145
Dropout rate (DR)	1.7050×10^{-2}
Learning rate (LR)	1.8521×10^{-3}
Weight decay rate (WD)	1.9480×10^{-5}
Simple graph neural network	
Embedding dimension (ED)	256
No. of convolutional layers (CL)	6
No. of hidden MLP layers (NL)	1
No. of hidden MLP neurons (HN)	144
Dropout rate (DR)	5.9461×10^{-2}
Learning rate (LR)	8.6572×10^{-4}
Weight decay rate (WD)	1.4280×10^{-5}
Attentive fingerprint	
Fingerprint size (FS)	195
No. of atom node layers (AL)	5
No. of super node layers (SL)	2
Dropout rate (DR)	1.237×10^{-1}
Learning rate (LR)	5.4619×10^{-4}
Weight decay rate (WD)	1.9332×10^{-5}

[a] first value - CEPDB, second value - HOPV15

Table A4: *Baseline models optimal hyperparameters for CEPDB dataset after 100 trials.*

Parameter name	Optimal parameter value
Fingerprint parameters (all baseline models)	
Fingerprint size (FS)	4096
Fingerprint radius (FR)	3
Fingerprint chirality (FC)	True
Fingerprint bond types (FB)	True
Support vector regression parameters	
SVR kernel (SK)	custom-rbf
Gamma kernel coefficient (GK)	3.2920×10^{-1}
Regularization parameter (CP)	1.7246×10^{1}
Epsilon parameter (EP)	9.1050×10^{-4}
Random forests parameters	
No. of trees (NT)	180
Max tree depth (MD)	83
Min samples split (MSS)	5
Min samples leaf (MSL)	1
Max features (MF)	0.1
Bootstrap (BS)	False
Max samples (MS)	6
High dimensional model representation parameters	
Polynomial order (PO)	6
HDMR order (HO)	2

References

[1] Dgl-LifeSci, last accessed 2020-12-16. https://github.com/awslabs/dgl-lifesci.

[2] RDKit: Open-source cheminformatics, last accessed 2020-12-16. https://www.rdkit.org.

[3] O. A. Abdulrazzaq, V. Saini, S. Bourdo, E. Dervishi, and A. S. Biris. Organic solar cells: a review of materials, limitations, and possibilities for improvement. *Particulate Science and Technology*, 31(5):427–442, 2013.

[4] T. Akiba, S. Sano, T. Yanase, T. Ohta, and M. Koyama. Optuna: A next-generation hyperparameter optimization framework. In *Proceedings of the 25rd ACM SIGKDD International Conference on Knowledge Discovery and Data Mining*, 2019.

[5] D. Bahdanau, K. Cho, and Y. Bengio. Neural machine translation by jointly learning to align and translate. *arXiv preprint arXiv:1409.0473*, 2014.

[6] L. Breiman. Random forests. *Machine Learning*, 45(1):5–32, 2001.

[7] K. Cho, B. Van Merriënboer, C. Gulcehre, D. Bahdanau, F. Bougares, H. Schwenk, and Y. Bengio. Learning phrase representations using RNN encoder-decoder for statistical machine translation. *arXiv preprint arXiv:1406.1078*, 2014.

[8] CMCL Innovations. MoDS (Model Development Suite), version 2020.2.2, 2020. https://cmclinnovations.com/products/mods/.

[9] D. K. Duvenaud, D. Maclaurin, J. Iparraguirre, R. Bombarell, T. Hirzel, A. Aspuru-Guzik, and R. P. Adams. Convolutional networks on graphs for learning molecular fingerprints. *Advances in Neural Information Processing Systems*, 28:2224–2232, 2015.

[10] J. Gilmer, S. S. Schoenholz, P. F. Riley, O. Vinyals, and G. E. Dahl. Neural message passing for quantum chemistry. *arXiv preprint arXiv:1704.01212*, 2017.

[11] M. A. Green, A. Ho-Baillie, and H. J. Snaith. The emergence of perovskite solar cells. *Nature Photonics*, 8(7):506–514, 2014.

[12] C. A. Gueymard, D. Myers, and K. Emery. Proposed reference irradiance spectra for solar energy systems testing. *Solar Energy*, 73(6):443–467, 2002.

[13] J. Hachmann, R. Olivares-Amaya, S. Atahan-Evrenk, C. Amador-Bedolla, R. S. Sánchez-Carrera, A. Gold-Parker, L. Vogt, A. M. Brockway, and A. Aspuru-Guzik. The Harvard clean energy project: large-scale computational screening and design of organic photovoltaics on the world community grid. *The Journal of Physical Chemistry Letters*, 2(17):2241–2251, 2011.

[14] S. Hochreiter and J. Schmidhuber. Long short-term memory. *Neural Computation*, 9(8):1735–1780, 1997.

[15] M. Jeong, I. W. Choi, E. M. Go, Y. Cho, M. Kim, B. Lee, S. Jeong, Y. Jo, H. W. Choi, J. Lee, et al. Stable perovskite solar cells with efficiency exceeding 24.8% and 0.3-v voltage loss. *Science*, 369(6511):1615–1620, 2020.

[16] D. P. Kingma and J. Ba. Adam: A method for stochastic optimization, 2017. URL https://arxiv.org/abs/1412.6980.

[17] T. N. Kipf and M. Welling. Semi-supervised classification with graph convolutional networks. *arXiv preprint arXiv:1609.02907*, 2016.

[18] G. Lambard and E. Gracheva. SMILES-x: autonomous molecular compounds characterization for small datasets without descriptors. *Machine Learning: Science and Technology*, 1(2):1–11, 2020. doi:10.1088/2632-2153/ab57f3.

[19] G. Landrum. Rdkit: A software suite for cheminformatics, computational chemistry, and predictive modeling, 2013.

[20] G. Li, S.-W. Wang, and H. Rabitz. Practical approaches to construct RS-HDMR component functions. *The Journal of Physical Chemistry A*, 106(37):8721–8733, 2002. doi:10.1021/jp014567t.

[21] Y. Li, D. Tarlow, M. Brockschmidt, and R. Zemel. Gated graph sequence neural networks. *arXiv preprint arXiv:1511.05493*, 2015.

[22] S. A. Lopez, E. O. Pyzer-Knapp, G. N. Simm, T. Lutzow, K. Li, L. R. Seress, J. Hachmann, and A. Aspuru-Guzik. The Harvard organic photovoltaic dataset. *Scientific Data*, 3(1):1–7, 2016.

[23] S. A. Lopez, B. Sanchez-Lengeling, J. de Goes Soares, and A. Aspuru-Guzik. Design principles and top non-fullerene acceptor candidates for organic photovoltaics. *Joule*, 1(4):857–870, 2017.

[24] N. Meftahi, M. Klymenko, A. J. Christofferson, U. Bach, D. A. Winkler, and S. P. Russo. Machine learning property prediction for organic photovoltaic devices. *npj Computational Materials*, 6(1):1–8, 2020.

[25] H. L. Morgan. The generation of a unique machine description for chemical structures-a technique developed at chemical abstracts service. *Journal of Chemical Documentation*, 5(2):107–113, 1965.

[26] S. Nagasawa, E. Al-Naamani, and A. Saeki. Computer-aided screening of conjugated polymers for organic solar cell: classification by random forest. *The Journal of Physical Chemistry Letters*, 9(10):2639–2646, 2018.

[27] D. Padula, J. D. Simpson, and A. Troisi. Combining electronic and structural features in machine learning models to predict organic solar cells properties. *Materials Horizons*, 6(2):343–349, 2019.

[28] F. Pedregosa, G. Varoquaux, A. Gramfort, V. Michel, B. Thirion, O. Grisel, M. Blondel, P. Prettenhofer, R. Weiss, V. Dubourg, J. Vanderplas, A. Passos, D. Cournapeau, M. Brucher, M. Perrot, and E. Duchesnay. Scikit-learn: Machine learning in Python. *Journal of Machine Learning Research*, 12:2825–2830, 2011.

[29] E. O. Pyzer-Knapp, K. Li, and A. Aspuru-Guzik. Learning from the Harvard clean energy project: The use of neural networks to accelerate materials discovery. *Advanced Functional Materials*, 25(41):6495–6502, 2015.

[30] E. O. Pyzer-Knapp, G. N. Simm, and A. A. Guzik. A Bayesian approach to calibrating high-throughput virtual screening results and application to organic photovoltaic materials. *Materials Horizons*, 3(3):226–233, 2016.

[31] H. Rabitz and Ö. F. Aliş. General foundations of high-dimensional model representations. *Journal of Mathematical Chemistry*, 25(2-3):197–233, 1999. doi:10.1023/A:1019188517934.

[32] D. Rogers and M. Hahn. Extended-connectivity fingerprints. *Journal of Chemical Information and Modeling*, 50(5):742–754, 2010.

[33] S. Rühle. Tabulated values of the Shockley–Queisser limit for single junction solar cells. *Solar Energy*, 130:139–147, 2016.

[34] S. Ryu, J. Lim, S. H. Hong, and W. Y. Kim. Deeply learning molecular structure-property relationships using attention-and gate-augmented graph convolutional network. *arXiv preprint arXiv:1805.10988*, 2018.

[35] H. Sahu and H. Ma. Unraveling correlations between molecular properties and device parameters of organic solar cells using machine learning. *The Journal of Physical Chemistry Letters*, 10(22):7277–7284, 2019.

[36] H. Sahu, F. Yang, X. Ye, J. Ma, W. Fang, and H. Ma. Designing promising molecules for organic solar cells via machine learning assisted virtual screening. *Journal of Materials Chemistry A*, 7(29):17480–17488, 2019.

[37] M. C. Scharber and N. S. Sariciftci. Efficiency of bulk-heterojunction organic solar cells. *Progress in Polymer Science*, 38(12):1929–1940, 2013.

[38] M. C. Scharber, D. Mühlbacher, M. Koppe, P. Denk, C. Waldauf, A. J. Heeger, and C. J. Brabec. Design rules for donors in bulk-heterojunction solar cells—towards 10% energy-conversion efficiency. *Advanced Materials*, 18(6):789–794, 2006.

[39] A. J. Smola and B. Schölkopf. A tutorial on support vector regression. *Statistics and Computing*, 14(3):199–222, 2004.

[40] H. J. Snaith. Perovskites: the emergence of a new era for low-cost, high-efficiency solar cells. *The journal of Physical Chemistry Letters*, 4(21):3623–3630, 2013.

[41] W. Sun, M. Li, Y. Li, Z. Wu, Y. Sun, S. Lu, Z. Xiao, B. Zhao, and K. Sun. The use of deep learning to fast evaluate organic photovoltaic materials. *Advanced Theory and Simulations*, 2(1):1800116, 2019.

[42] W. Sun, Y. Zheng, K. Yang, Q. Zhang, A. A. Shah, Z. Wu, Y. Sun, L. Feng, D. Chen, Z. Xiao, et al. Machine learning–assisted molecular design and efficiency prediction for high-performance organic photovoltaic materials. *Science Advances*, 5(11):1–8, 2019. doi:10.1126/sciadv.aay4275.

[43] A. Urbina. The balance between efficiency, stability and environmental impacts in perovskite solar cells: a review. *Journal of Physics: Energy*, 2(2):1–25, 2020. doi:10.1088/2515-7655/ab5eee.

[44] K. Vandewal, S. Himmelberger, and A. Salleo. Structural factors that affect the performance of organic bulk heterojunction solar cells. *Macromolecules*, 46(16): 6379–6387, 2013.

[45] P. Veličković, G. Cucurull, A. Casanova, A. Romero, P. Lio, and Y. Bengio. Graph attention networks. *arXiv preprint arXiv:1710.10903*, 2017.

[46] M. Wang, D. Zheng, Z. Ye, Q. Gan, M. Li, X. Song, J. Zhou, C. Ma, L. Yu, Y. Gai, T. Xiao, T. He, G. Karypis, J. Li, and Z. Zhang. Deep graph library: A graph-centric, highly-performant package for graph neural networks. *arXiv preprint arXiv:1909.01315*, 2019.

[47] B. Weisfeiler and A. Lehmann. A reduction of a graph to a canonical form and an algebra arising during this reduction. *Nauchno-Technicheskaya Informatsia*, 2(9): 12–16, 1968.

[48] D. Wöhrle and D. Meissner. Organic solar cells. *Advanced Materials*, 3(3):129–138, 1991.

[49] J. Wu, S. Wang, L. Zhou, X. Ji, Y. Dai, Y. Dang, and M. Kraft. Deep-learning architecture in QSPR modeling for the prediction of energy conversion efficiency of solar cells. *Industrial & Engineering Chemistry Research*, 2020.

[50] Z. Wu, B. Ramsundar, E. N. Feinberg, J. Gomes, C. Geniesse, A. S. Pappu, K. Leswing, and V. Pande. MoleculeNet: a benchmark for molecular machine learning. *Chemical Science*, 9(2):513–530, 2018.

[51] Y. Xie, W. Wang, W. Huang, F. Lin, T. Li, S. Liu, X. Zhan, Y. Liang, C. Gao, H. Wu, et al. Assessing the energy offset at the electron donor/acceptor interface in organic solar cells through radiative efficiency measurements. *Energy & Environmental Science*, 12(12):3556–3566, 2019.

[52] Z. Xiong, D. Wang, X. Liu, F. Zhong, X. Wan, X. Li, Z. Li, X. Luo, K. Chen, H. Jiang, et al. Pushing the boundaries of molecular representation for drug discovery with the graph attention mechanism. *Journal of Medicinal Chemistry*, 2019.

[53] Z. Xu, L.-M. Chen, M.-H. Chen, G. Li, and Y. Yang. Energy level alignment of poly (3-hexylthiophene):[6, 6]-phenyl c 61 butyric acid methyl ester bulk heterojunction. *Applied Physics Letters*, 95(1):178, 2009.

[54] Z.-W. Zhao, M. del Cueto, Y. Geng, and A. Troisi. Effect of increasing the descriptor set on machine learning prediction of small molecule-based organic solar cells. *Chemistry of Materials*, 32(18):7777–7787, 2020.